Supporting Information

Hole Transporting Materials Based on Benzodithiophene and Dithienopyrrole Cores for Efficient Perovskite Solar Cells

Rafael Sandoval-Torrientes,[a] Iwan Zimmermann,[b] Joaquín Calbo,[c] Juan Aragó,[c] José Santos,[a] Enrique Ortí,*[c] Nazario Martín,*[a,d] Mohammad Khaja Nazeeruddin*[b]

[a] IMDEA-Nanociencia, Ciudad Universitaria de Cantoblanco, Madrid, 28049, Spain
[b] EPFL VALAIS, Sion, 1951, Switzerland
[c] Instituto de Ciencia Molecular, Universidad de Valencia, Paterna, 46980, Spain
[d] Facultad de Ciencias Químicas, Universidad Complutense de Madrid, Madrid, 28040, Spain.

Index

1. Experimental Section

General Methods. Chemicals and reagents were purchased from commercial suppliers and used as received. All solvents were dried according to standard procedures. Air-sensitive reactions were carried out under nitrogen atmosphere. The device preparation was done in a glovebox under nitrogen atmosphere. Flash chromatography was performed using silica gel (Fluorochem, Silicagel 60A, 40-63 micron). Analytical thin layer chromatography (TLC) was performed using aluminum-coated Merck Kieselgel 60 F254 plates. NMR spectra were recorded on a Bruker Advance 300 (^{1}H: 400 MHz; ^{13}C: 101 MHz) spectrometer at 298 K using partially deuterated solvents as internal standards. Coupling constants (*J*) are denoted in Hz and chemical shifts (δ) in ppm. Multiplicities are denoted as follows: s = singlet, d = doublet, t = triplet, m = multiplet. UV-vis spectra were recorded in a Varian Cary 50 spectrophotometer. FT-IR spectra were recorded on a Bruker Tensor 27 (ATR device) spectrometer. Photoluminescence (PL) spectra were performed on a Fluorolog-3 HORIBA spectrofluorometer. Mass spectra Matrix assisted Laser desorption ionization (coupled to a Time-of-Flight analyzer) experiments (MALDI-TOF) were recorded on a MAT 95 thermo spectrometer and a Bruker REFLEX spectrometer respectively. Thermogravimetric analysis (TGA) was performed using a TA Instruments TGAQ500 with a ramp of 10 °C/min under N_2 from 100 to 1000 °C. Differential scanning calorimetry (DSC) was run on a Discovery DSC from TA instruments. Three cycles were recorded under nitrogen, heating (until 400 °C) and cooling (50 °C) at 20 °C/min of scanning rate. Cyclic voltammetry (CV) experiments were performed in deaerated 0.1 M Bu_4NPF_6 DCM solutions at a scan rate of 100 mV s^{-1}. Glassy carbon was used as a working electrode and platinum wires as counter and reference electrodes. Before each measurement, solutions were deoxygenated with N_2. Ferrocene was added as an internal standard; its oxidation potential in DCM was set at 0.7 V *vs.* NHE and materials oxidation potentials were recalculated in reference to NHE.

2. Synthetic details and characterization.

Compounds **1** and **5** were purchased from commercial suppliers. Compounds **3**, **6** and 4-(4,4,5,5-tetramethyl-1,3,2-dioxaborolan-2-yl)-N,N-bis(4 methoxyphenyl)aniline (**4**) were synthesized following previously reported procedures.[1–3]

TTPA-DTP

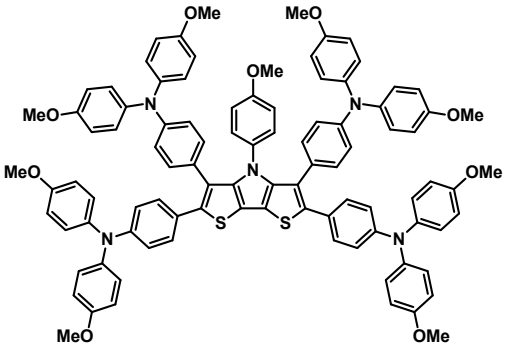

A solution of **3** (174 mg, 0.29 mmol), **4** (626 mg, 1.45 mmol), K_3PO_4 (1.47 g, 6.96 mmol) and $Pd(PPh_3)_4$ (60 mg, 0.06 mmol) in anhydrous DMF (20 mL) was degassed for 1 h under nitrogen and, thereafter, stirred at 100 °C for 18 h. Upon cooling to room temperature, water was added and the resulting precipitate filtered off, thoroughly washed with water, and then redissolved in hot chloroform. After drying the solution over anhydrous sodium sulfate, the solvent was removed under reduced pressure and the crude product purified by flash chromatography on silica gel using toluene/EtOAc (100:3) as eluent to give **TTPA-DTP** as an orange solid (780 mg, 60%). mp 288−290 °C; ^{1}H NMR (400 MHz, THF-d_8, δ): 7.06–7.03 (m, 4H, Ar H), 7.02–6.99 (m, 8H, Ar H), 6.94–6.90 (m, 8H, Ar H), 6.85–6.79 (m, 16H, Ar H), 6.72–6.62 (m, 10H, Ar H), 6.52–6.45 (m, 6H, Ar H), 3.83 (s, 3H, OCH_3), 3.75 (s, 12H, OCH_3), 3.74 (s, 12H, OCH_3); ^{13}C NMR (101 MHz, THF-d_8, δ): 159.6, 157.5, 157.2, 148.6, 148.2, 145.4, 141.9, 141.6, 138.0, 131.8, 130.8, 130.0, 128.6, 127.8, 127.4, 125.2, 120.4, 120.2, 115.6, 115.5, 114.2, 113.7, 56.2, 55.7; FTIR (neat): 2924, 2853, 1718, 1605, 1504, 1464, 1320, 1279, 1240, 1174, 1106, 1034, 827, 728, 575 cm^{-1}; HRMS (MALDI-TOF) *m/z*: calcd for $C_{95}H_{79}N_5O_9S_2$, 1497.5314; found, 1497.5259.

TTPA-BDT

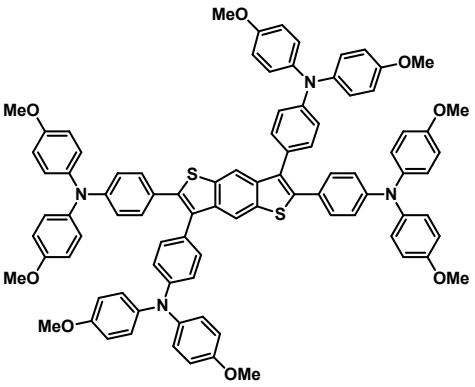

A solution of **6** (101 mg, 0.20 mmol), **4** (362 mg, 0.84 mmol), K_3PO_4 (1.02 g, 4.80 mmol) and $Pd(PPh_3)_4$ (46 mg, 0.04 mmol) in anhydrous DMF (150 mL) was degassed for 1h under nitrogen and, thereafter, stirred at 100 °C for 4 h. Upon cooling to room temperature, water was added and the resulting precipitate filtered off, thoroughly washed with

water, and then redissolved in hot chloroform. After drying the solution over anhydrous sodium sulfate, the solvent was removed under reduced pressure and the crude product purified by flash chromatography on silica gel using CH_2Cl_2 and then, CH_2Cl_2/EtOAc (200:1) as eluent to give **TTPA-BDT** as a light-yellow solid (168 mg, 60%). mp 206−208 °C; ^{1}H NMR (400 MHz, THF-d_8, δ): 7.93 (s, 2H, Ar H), 7.18 (d, *J* = 6.4 Hz, 4H, Ar H), 7.16 (d, *J* = 6.1 Hz, 4H, Ar H), 7.13–7.08 (m, 8H, Ar H), 7.07–7.01 (m, 8H, Ar H), 6.96 (d, *J* = 8.7 Hz, 4H, Ar H), 6.88–6.82 (m, 16H, Ar H), 6.74 (d, *J* = 8.8 Hz, 4H, Ar H), 3.76 (s, 12H, OCH_3), 3.75 (s, 12H, OCH_3); ^{13}C NMR (101 MHz, THF-d_8, δ): 157.8, 157.6, 149.6, 149.4, 141.8, 141.4, 140.8, 140.4, 136.8, 131.9, 130.7, 128.5, 128.1, 128.0, 127.0, 125.3, 120.8, 119.7, 116.6, 115.7, 55.8; FTIR (neat): 3038, 2999, 2927, 2837, 1741, 1605, 1502, 1463, 1319, 1281, 1239, 1175, 1106, 1034, 826, 729, 603, 575 cm^{-1}; HRMS (MALDI-TOF) *m/z*: calcd for $C_{90}H_{74}N_4O_8S_2$, 1402.4943; found, 1402.4932.

3. Computational details.

Quantum-chemical calculations were carried out with the Gaussian 09 (revision D.01) software package.[4] All the calculations were performed within the density functional theory (DFT) framework using the B3LYP functional[5] and the 6-31G** basis set.[6] Solvent effects were considered within the self-consistent reaction field (SCRF) theory by using the polarized continuum model (PCM) approach.[7] C_2 symmetry constraints were imposed during the optimizations of **TTPA-BDT** and its core (BDT) respectively, whereas no symmetry constraints were used to calculate **TTPA-DTP** and the DTP core. The TPA substituent was also optimized under C_2 symmetry. Vertical electronic transition energies to the lowest-energy singlet excited states of **TTPA-BDT** and **TTPA-DTP** were computed by using the time-dependent density functional theory (TDDFT) approach.[8] The lowest 50 singlet excited states were calculated at the B3LYP/6-31G** level using the ground-state optimized geometries. Geometry optimizations in gas phase of the radical cations of **TTPA-BDT** and **TTPA-DTP**, and their BDT and DTP cores were also performed to evaluate the reorganization energy (the evaluation process is explained below). For the electrochemical properties, radical cations are treated as open-shell systems and computed within the spin-unrestricted DFT approximation at the UB3LYP/6-31G** level in the presence of CH_2Cl_2. Additionally, dication, trication and tetracation species were also computed in CH_2Cl_2. Molecular orbitals were plotted using the Chemcraft 1.6 software with isovalue contours of ±0.03 a.u.[9]

Figure S1 shows the B3LYP/6-31G**-optimized values calculated for selected bond lengths of the BDT and DTP cores and the **TTPA-BDT** and **TTPA-DTP** HTMs. Figure S2 displays the optimized structures of the four-armed HTMs. Figure S3 depicts the topology and energy of the frontier molecular orbitals participating in the electronic transitions to the lowest-energy singlet excited states.

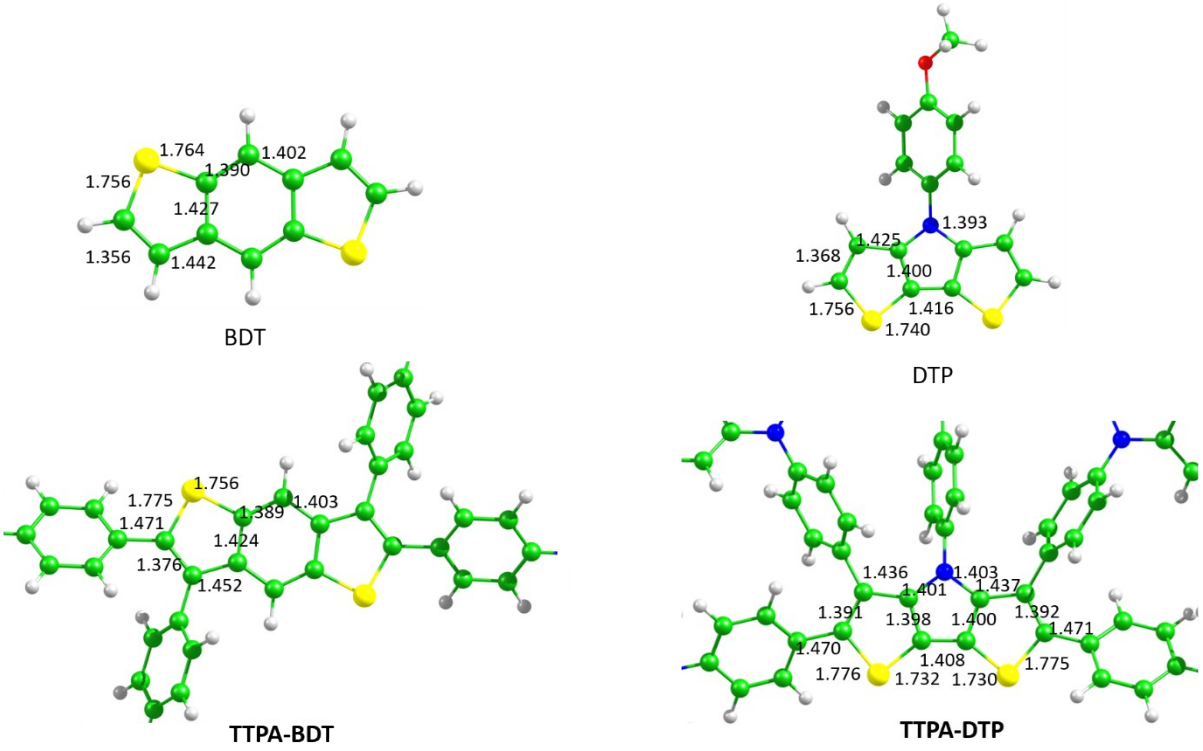

Figure S1. Optimized bond lengths (in Å) calculated at the B3LYP/6-31G** level, in CH_2Cl_2 solution, for the BDT and DTP cores and for the **TTPA-BDT** and **TTPA-DTP** compounds. For the latter, the terminal TTPA pendant groups have been partially omitted and only the bond lengths calculated for the cores are shown.

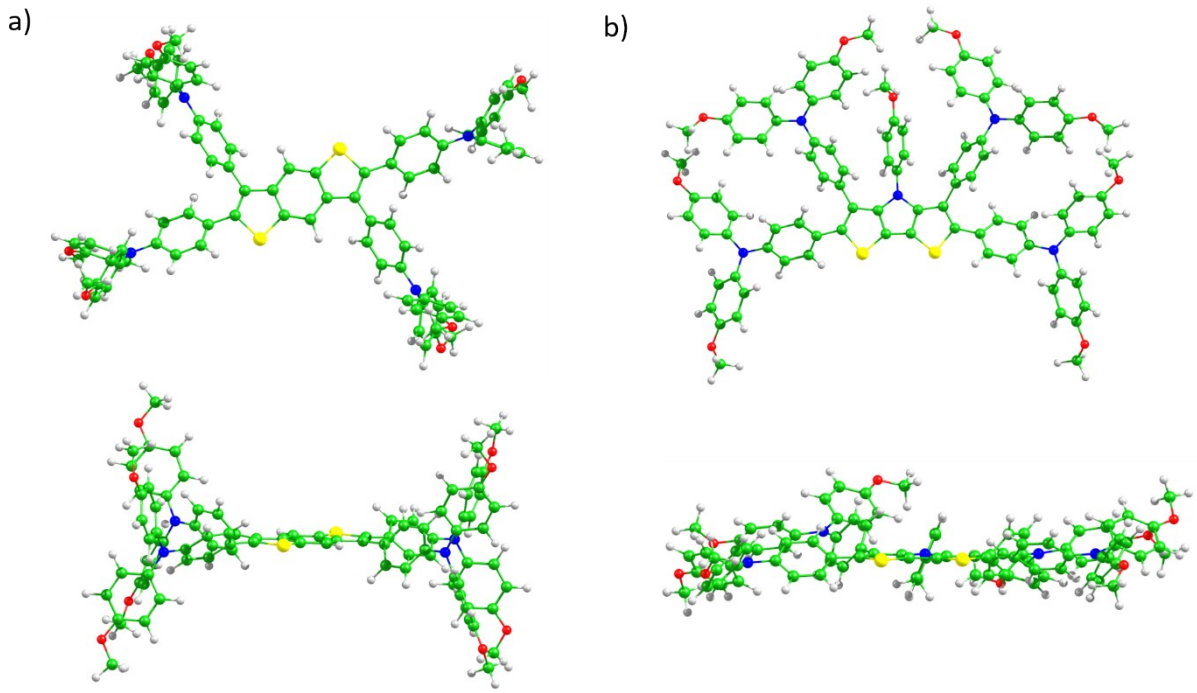

Figure S2. Top and side views of the minimum-energy optimized geometries calculated at the B3LYP/6-31G** level for **TTPA-BDT** (a) and **TTPA-DTP** (b).

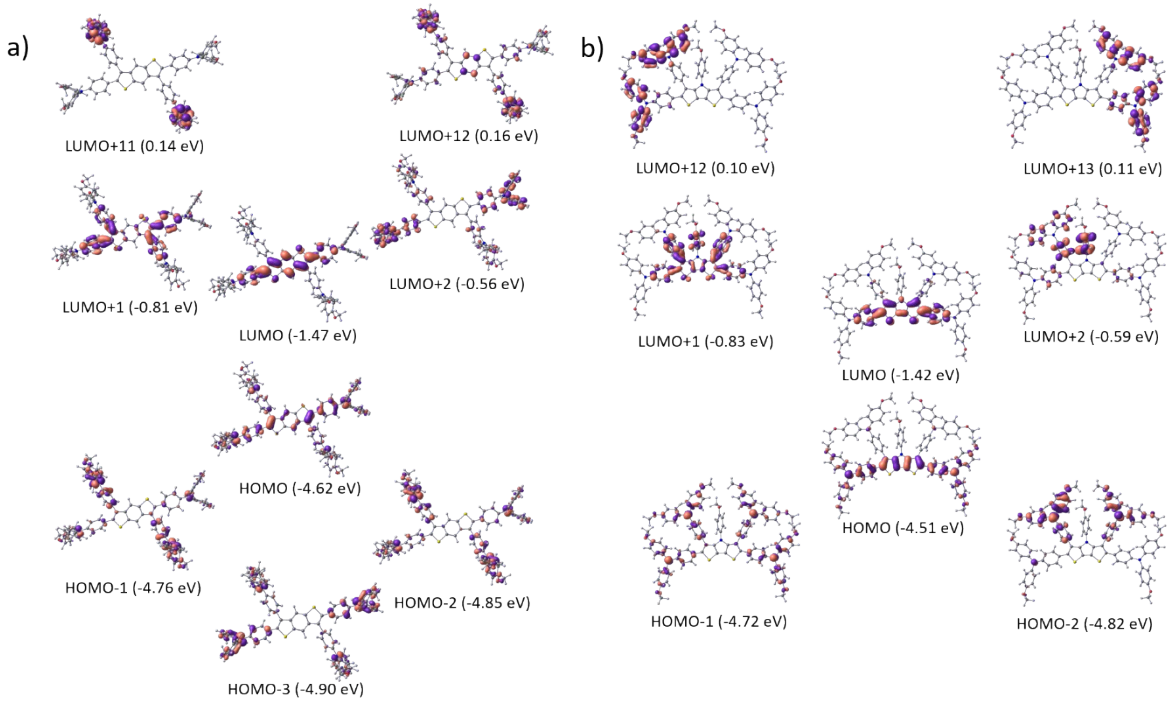

Figure S3. Isovalue contours (±0.03 a.u.) and energies calculated at the B3LYP/6-31G** level in CH_2Cl_2 for selected molecular orbitals of **TTPA-BDT** (a) and **TTPA-DTP** (b).

Oxidized species. B3LYP/6-31G** calculations in CH_2Cl_2 were used to investigate the molecular structure and the charge distribution of the four-armed HTMs in different oxidation states, from the monocation to the tetracation. Cation species were computed to be doublet open-shell species. Dications of **TTPA-BDT** and **TTPA-DTP** were calculated as singlet closed-shell species, in which both electrons are extracted from the same orbital, and triplet open-shell species, in which the electrons are extracted from different orbitals. For [**TTPA-BDT**]$^{2+}$ and [**TTPA-DTP**]$^{2+}$ the triplet state was found to be more stable than the singlet state by 0.19 eV and 0.04 eV, respectively. In the case of trications, doublet and quadruplet open-shell states were computed. For [**TTPA-BDT**]$^{3+}$, the quadruplet state turned out to be the most stable by 0.28 eV with respect to the doublet. In contrast, for [**TTPA-DTP**]$^{3+}$, the doublet and quadruplet states are almost degenerate in energy; the doublet being the more stable by 0.007 eV. For [**TTPA-BDT**]$^{4+}$, the quintet state is the most stable state by 0.607 and 0.749 eV compared to the triplet and singlet states, respectively. For [**TTPA-DTP**]$^{4+}$, the triplet and quintet states were found to be almost degenerate, the triplet being more stable by 0.009 eV whereas the singlet state is higher in energy by 0.558 eV in comparison with the triplet state. Table S1 gathers the Mulliken atomic charges computed for the cores and the peripheral TPA groups of the different oxidized species of **TTPA-BDT** and **TTPA-DTP** in their most stable electronic state.

Table S1. Mulliken atomic charges (in e) computed for the BDT and DTP cores and for the TPA groups of **TTPA-BDT** and **TTPA-DTP** in different oxidized states.

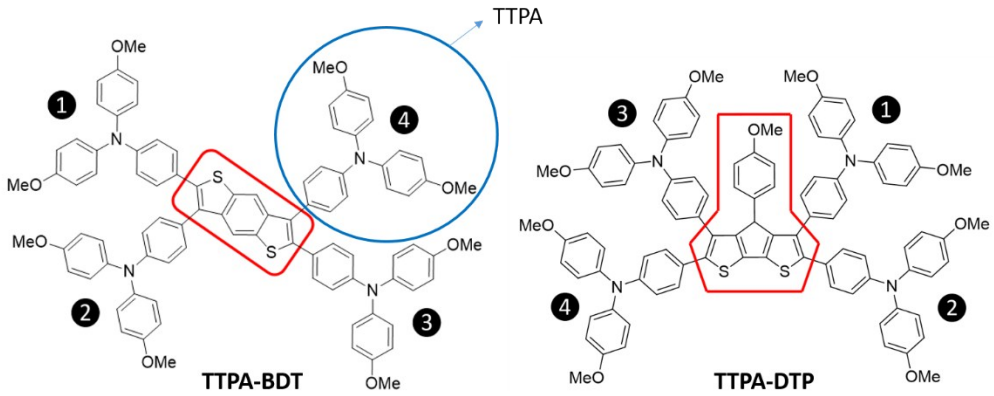

Compound	Neutral	Cation	Dication	Trication	Tetracation
TTPA-BDT					
BDT	−0.257	−0.123	−0.094	−0.075	−0.051
TPA-1	0.101	0.343	0.571	0.816	1.049
TPA-2	0.028	0.218	0.476	0.721	0.976
TPA-3	0.101	0.343	0.571	0.816	1.049
TPA-4	0.028	0.218	0.476	0.721	0.976
TTPA-DTP					
DTP	−0.185	0.021	0.031	0.042	0.053
TPA-1	0.007	0.100	0.364	0.618	0.939
TPA-2	0.084	0.388	0.621	0.868	1.027
TPA-3	0.011	0.098	0.349	0.596	0.954
TPA-4	0.082	0.393	0.635	0.876	1.028

Figure S4 represents the potential energy surfaces for the neutral and cation states of two molecules (labelled as 1 and 2) involved in a charge transfer process. The intramolecular reorganization energy (λ) consists of two terms related to the geometry relaxation energies of one molecule going from the fully relaxed ground state of the neutral species to the cation state (Figure S4, left) and a neighbouring molecule evolving in the opposite way (Figure S4, right),

$$\lambda = \lambda_1 + \lambda_2 \qquad \text{* MERGEFORMAT (1)}$$

$$\lambda_1 = E(M1) - E(M1^+) \qquad \text{* MERGEFORMAT (2)}$$

$$\lambda_2 = E(M2^+) - E(M2) \qquad \text{* MERGEFORMAT (3)}$$

Here, E(M1) and E(M1$^+$) for molecule 1 are the energies of the positively charged molecule (the cation) at the equilibrium geometry of the neutral molecule and the relaxed cation, respectively, and E(M2$^+$) and E(M2) for molecule 2 are, accordingly, the energies of the neutral molecule at the equilibrium geometry of the cation and the neutral molecule, respectively.

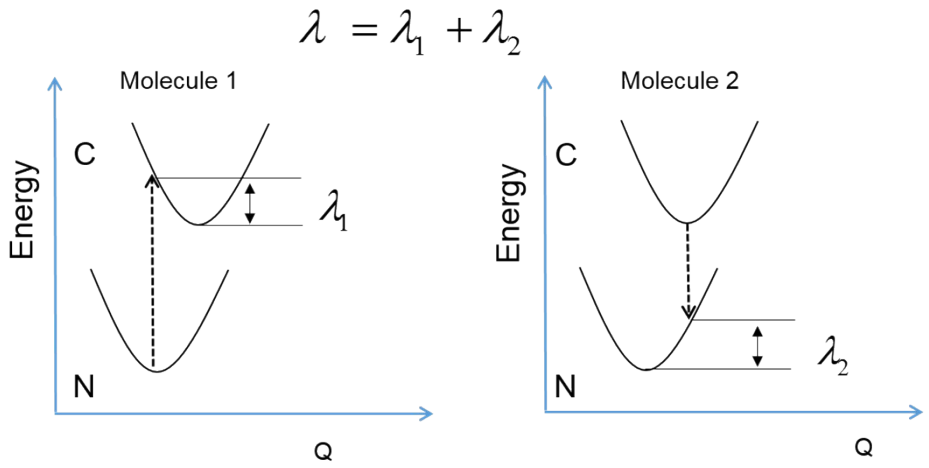

Figure S4. Scheme of the potential energy surfaces of the neutral state (N) and the cation state (C) for two molecules (1 and 2) involved in a charge (hole) transfer process. λ_1 and λ_2 are the two contributions to the total intramolecular reorganization energy (λ).

Figure S5 displays the theoretical absorption spectra calculated for **TTPA-BDT** and **TTPA-DTP** from the electronic transitions computed at the TDDFT B3LYP/6-31G** level in CH_2Cl_2 solution. Table S2 gathers the vertical excitation energies (*E*), the oscillator strengths (*f*) and the electronic descriptions in terms of one-electron molecular orbital excitations calculated in CH_2Cl_2 solution for the most relevant $S_0 \rightarrow S_n$ electronic transitions of **TTPA-BDT** and **TTPA-DTP**. Figure S3 shows the molecular orbitals involved in the $S_0 \rightarrow S_n$ transitions quoted in Table S2.

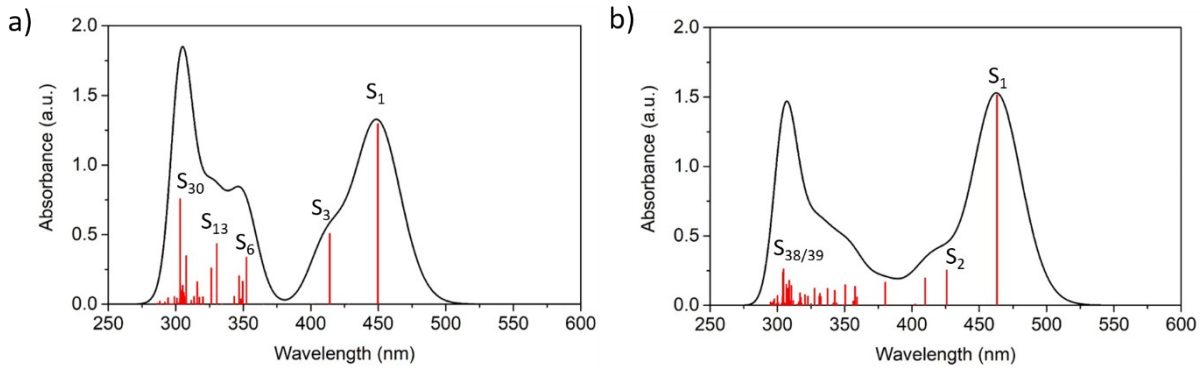

Figure S5. Stick and convoluted absorption spectra computed for **TTPA-BDT** (a) and **TTPA-DTP** (b) at the TDDFT B3LYP/6-31G** level in CH_2Cl_2. The TDDFT stick spectra were convoluted with Gaussian functions of full-width at half maximum (FWHM) = 0.15 eV.

Table S2. Lowest singlet excited states calculated at the TDDFT B3LYP/6-31G** level for **TTPA-BDT** and **TTPA-DTP** in CH_2Cl_2 solution. Vertical excitation energies (*E*), oscillator strengths (*f*), and dominant monoexcitations with contributions (within parentheses) greater than 10%.

Compound	State	*E* (eV/nm)	*f*	Description[a]
TTPA-BDT	S_1	2.76 / 450	1.295	H → L (97)
	S_3	2.99 / 414	0.507	H−2 → L (97)
	S_6	3.52 / 352	0.335	H−1 → L+1 (51)
	S_{13}	3.75 / 330	0.433	H−3 → L+1 (89)
	S_{30}	4.09 / 303	0.755	H−1 → L+12 (22)
				H → L+11 (15)
TTPA-DTP	S_1	2.68 / 463	1.513	H → L (96)
	S_3	2.91 / 426	0.252	H−1 → L (97)
	S_{38}	4.07 / 305	0.261	H → L+13 (15)
				H−1 → L+12 (11)
	S_{39}	4.08 / 304	0.238	H → L+13 (17)
				H−1 → L+13 (15)

[a] H and L denote HOMO and LUMO, respectively.

4. Device preparation / techniques

Conductive fluorine-doped tin oxide (FTO) glass (NSG10) was sequentially cleaned by sonication in a 2 % Helmanex solution and isopropanol for 15 min, respectively. A 30 nm titania blocking layer was applied on the substrates by spraying a solution of titanium diisopropoxide bis(acetylacetonate) in ethanol at 450 °C. For the 200–300 nm mesoporous TiO_2 layer, 30 NR-D titania paste from Dyesol diluted in ethanol (ratio 1:8 by weight) was applied by spin-coating at 2000 rpm for 10 s followed by a sintering step at 500 °C for 20 min. After cooling down the substrates, a Li-treatment was applied by spin-coating 60 µL of a solution of lithium tris(bis(trifluoromethylsulfonyl)imide) (Li-TFSI) in acetonitrile (10 mg/mL) onto the mesoporous layer, followed by a sintering step at 500 °C for 10 min to decompose the Li-salt as previously described.[10] The perovskite layers were fabricated by a single-step spin-coating procedure reported by Seok et al.[11] For the perovskite precursor solution 508 mg of PbI_2(TCI), 68 mg of PbI_2 (TCI), 180.5 mg of formamidinium iodide (Dyesol) and 20.7 mg of methylammonium bromide (Dyesol) were dissolved in a 1:4 mixture of DMSO:DMF. The perovskite solution was spun at 5000 rpm for 30 s using a ramp of 3000 rpm s^{-1}. 15 s prior to the end of the spin-coating sequence 100 µL of chlorobenzene were poured onto the spinning substrate. Afterwards, the substrates were transferred onto a heating plate and annealed at 100 °C for 45 min. The hole-transporting materials were applied from solutions in chlorobenzene. Optimized concentrations were found to be 30 mM for **TTPA-BDT** and **TTPA-DTP** and 70 mM for spiro-OMeTAD respectively. Tert-butylpyridine (Tbp), tris(2-(1H-pyrazol-1-yl)-4-tert-butylpyridine)cobalt(III) (FK209) and Li-TFSI were added as additives. Equimolar amounts of additives were added for all hole-transporters: 330 mol% Tbp, 50 mol% Li-TFSI from a 1.8M stock solution in acetonitrile and 6 mol% FK209 from a 0.25 M stock solution in acetonitrile. The final HTM solutions were spin-coated dynamically onto the perovskite layers at 4000 rpm for 20 s. The gold electrodes were deposited by thermal evaporation of 100 nm gold using a shadow mask under high vacuum conditions. All devices in this paper have been characterized after storage for one week in dry air under dark conditions.

4.1 Solar cell characterization

The photovoltaic device performance was analyzed using a VeraSol LED solar simulator (Newport) producing 1 sun AM 1.5 (100 W cm^{-2}) sunlight. Current density-voltage curves were measured in air with a potentiostat (Keithley). The light intensity was calibrated with an NREL certified KG5 filtered Si reference diode. The solar cells were masked with a metal aperture of 0.16 cm^2 to define the active area. The current-voltage curves were recorded scanning at 20 mV s^{-1}. Incident photon-to-current

efficiency (IPCE) measurements were performed on an IQE-200B quantum efficiency measurement system from Newport.

4.2 SEM

High resolution SEM images were taken using a FEI Teneo microscope.

4.3 PL measurements

Time-resolved PL experiments were performed with a spectrophotometer (Gilden Photonics) using a pulsed source at 460 nm (Ps diode lasers BDS-SM, pulse with < 100 ps, from Photonic Solutions, approx. 2 mW power, 20 MHz repetition rate, approx. 500 µm spot radius) and the signal was recorded at 785 nm by the Time Correlated Single Photon Counting detection technique with a time resolution of 1 ns. The glass/perovskite/HTM samples were excited from the HTM side under ambient conditions. All the samples have been encapsulated in inert atmosphere.

5. Solar cell characterization

5.1 EQE

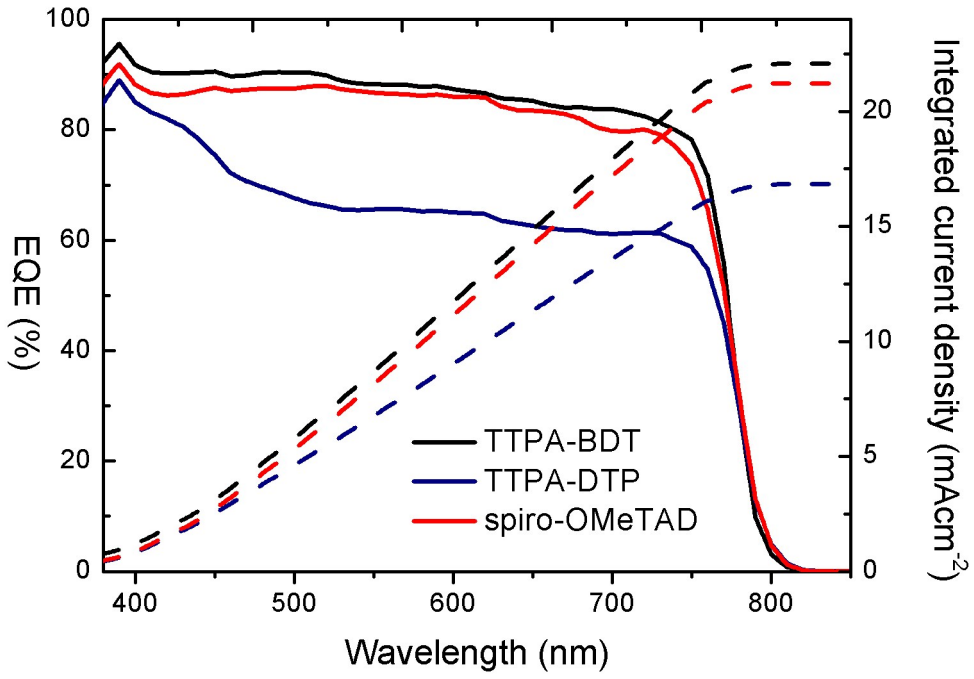

Figure S6. EQE (left axis) and integrated current density (right axis) wavelength dependency.

5.2 HTM film morphology

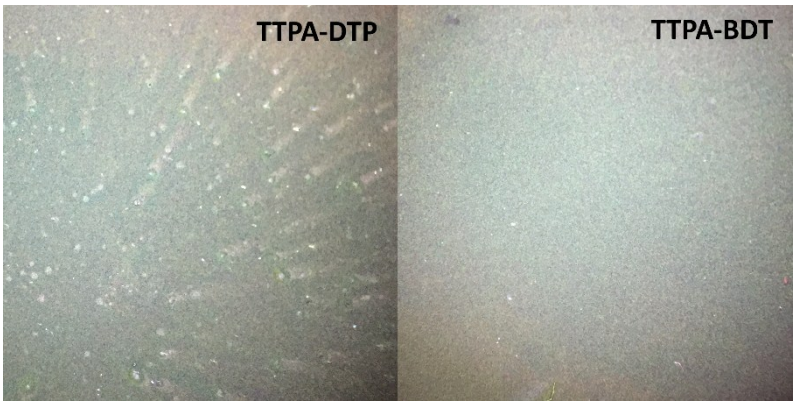

Figure S7. Images taken with optical microscope show the difference in morphology between **TTPA-BDT** and **TTPA-DTP**.

5.3 Photoluminescence

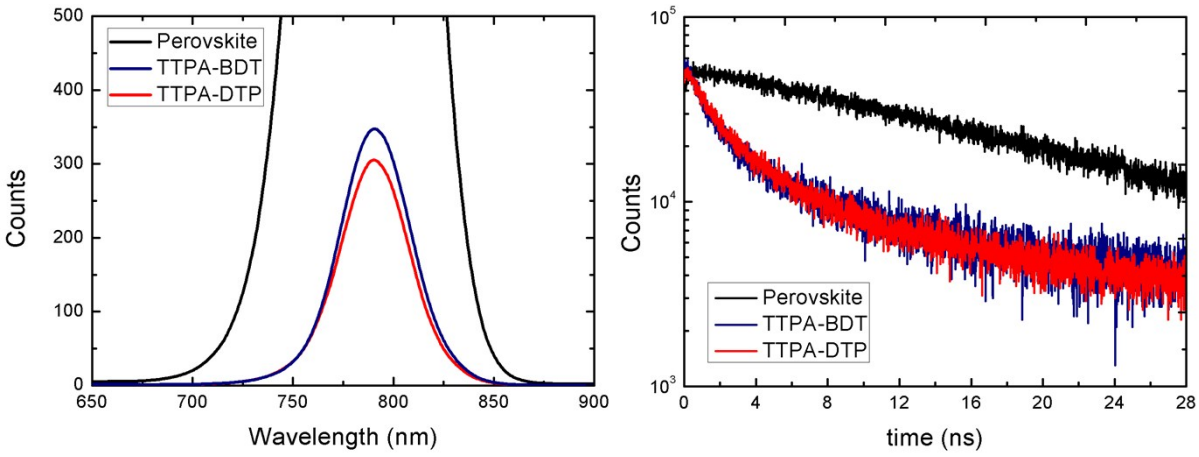

Figure S8. Steady state photoluminescence (ST-PL, left) and transient photoluminescence (TR-PL, right) of **TTPA-BDT** and **TTPA-DTP**. The excitation wavelength was at 500 nm for the ST-PL and 460 nm for the TR-PL.

5.4 Statistical Values

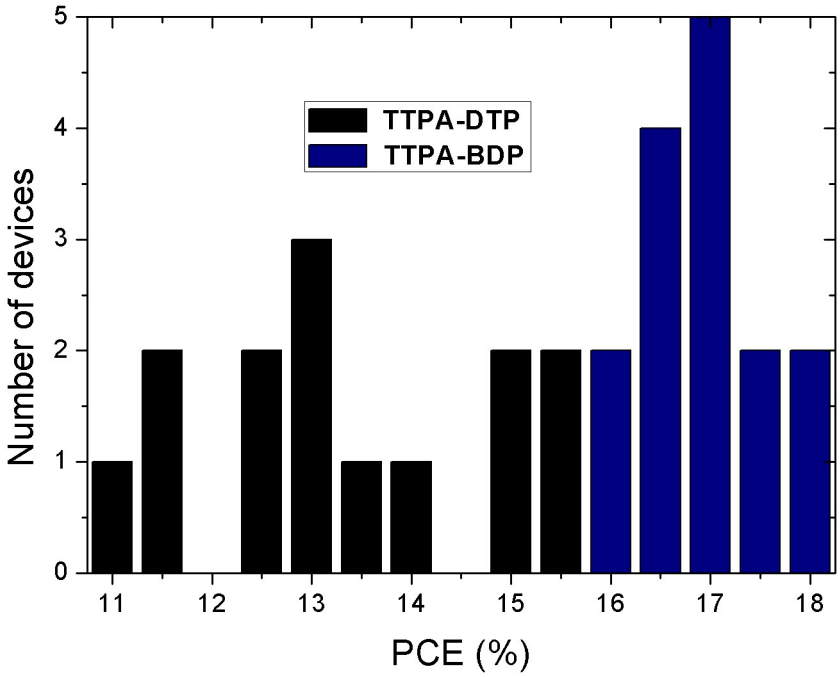

Figure S9. Statistical values of the 15 cells fabricated per novel HTM. Average PCE values are 16.98% for **TTPA-BDP** and 13.34% for **TTPA-DTP**.

6. Supplementary figures

6.1 NMR, MS

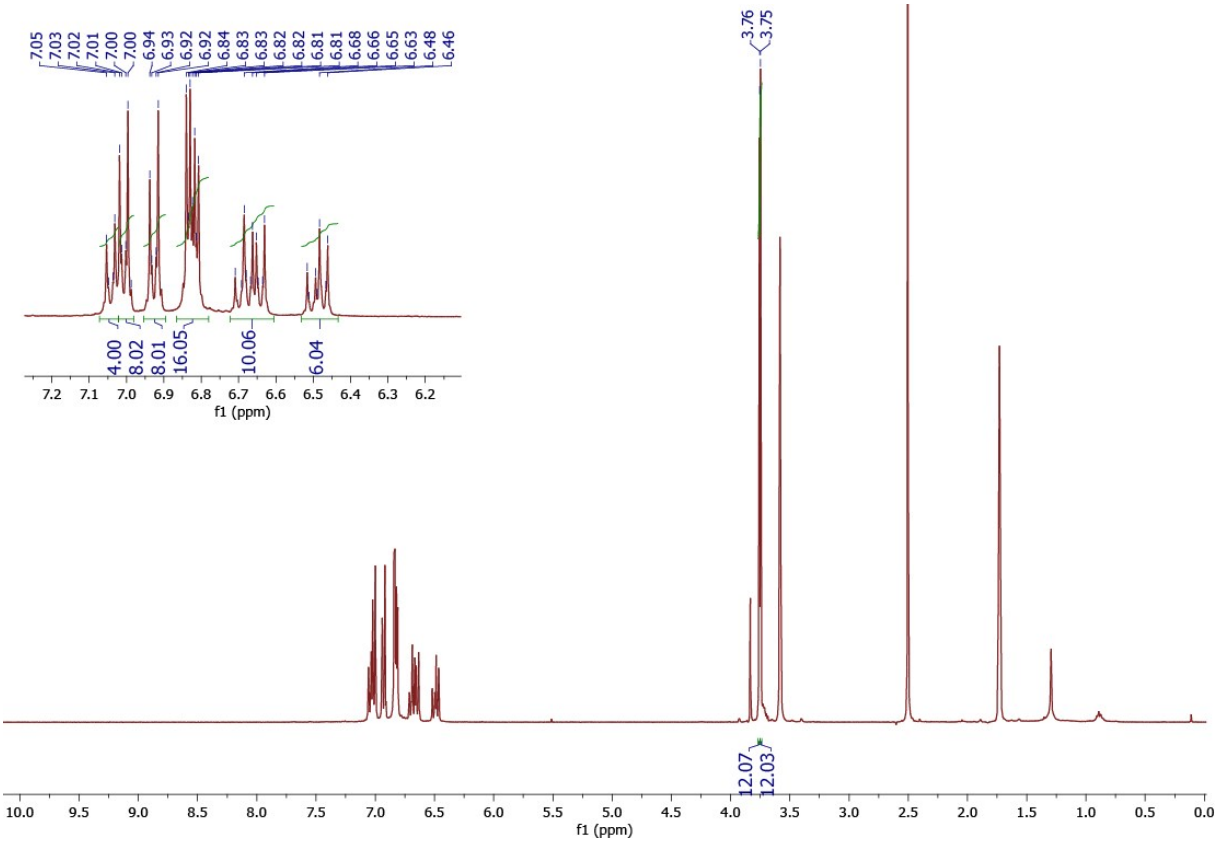

Figure S9. ^{1}H NMR (400 MHz, THF-d_8, 298 K) of compound **TTPA-DTP**.

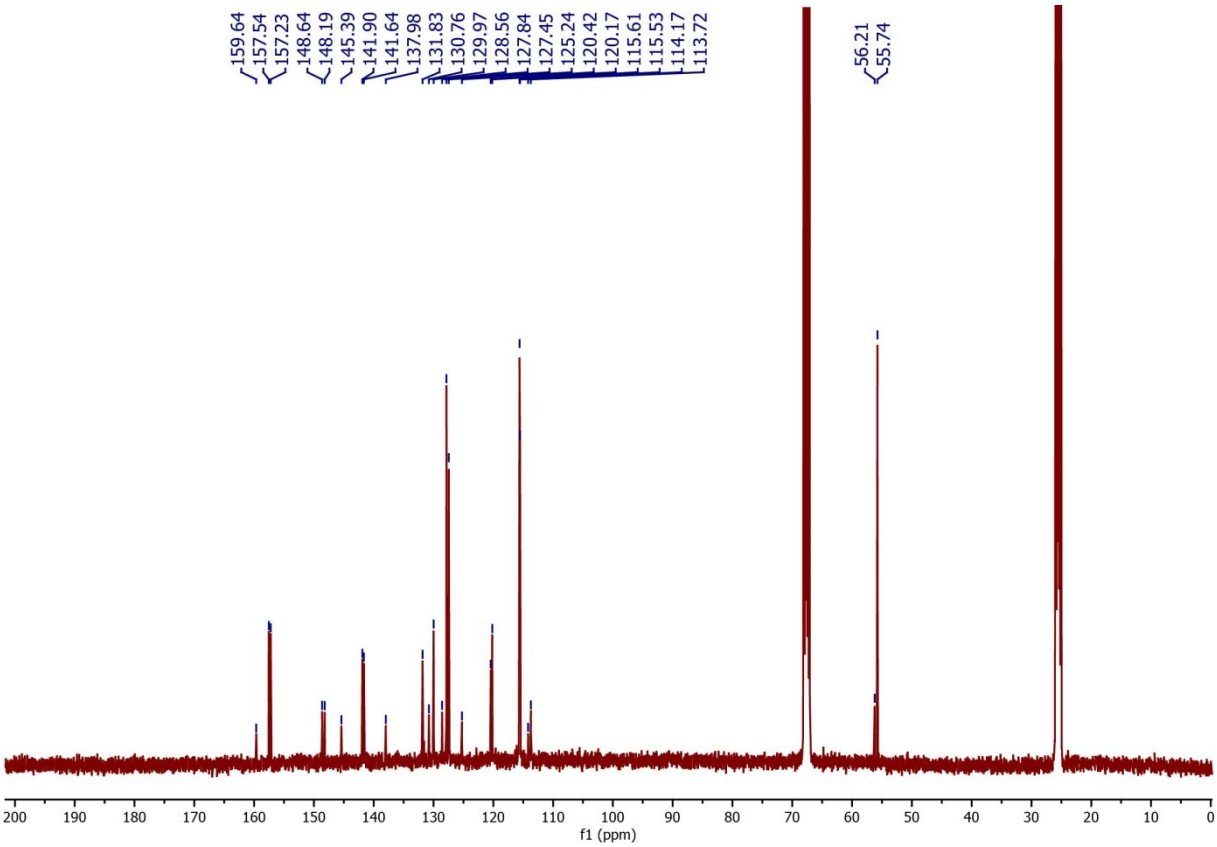

Figure S10. ^{13}C NMR (176 MHz, THF-d_8, 298 K) of compound **TTPA-DTP**.

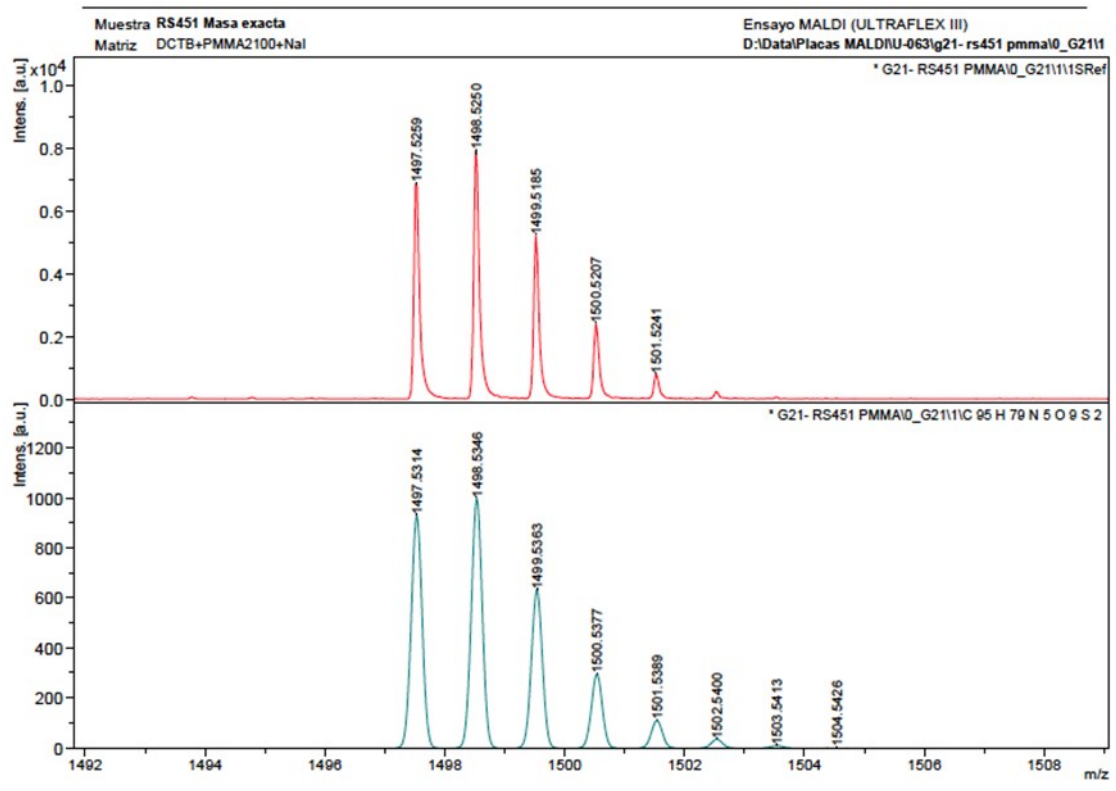

Figure S11. MALDI-TOF mass spectrum of **TTPA-DTP**.

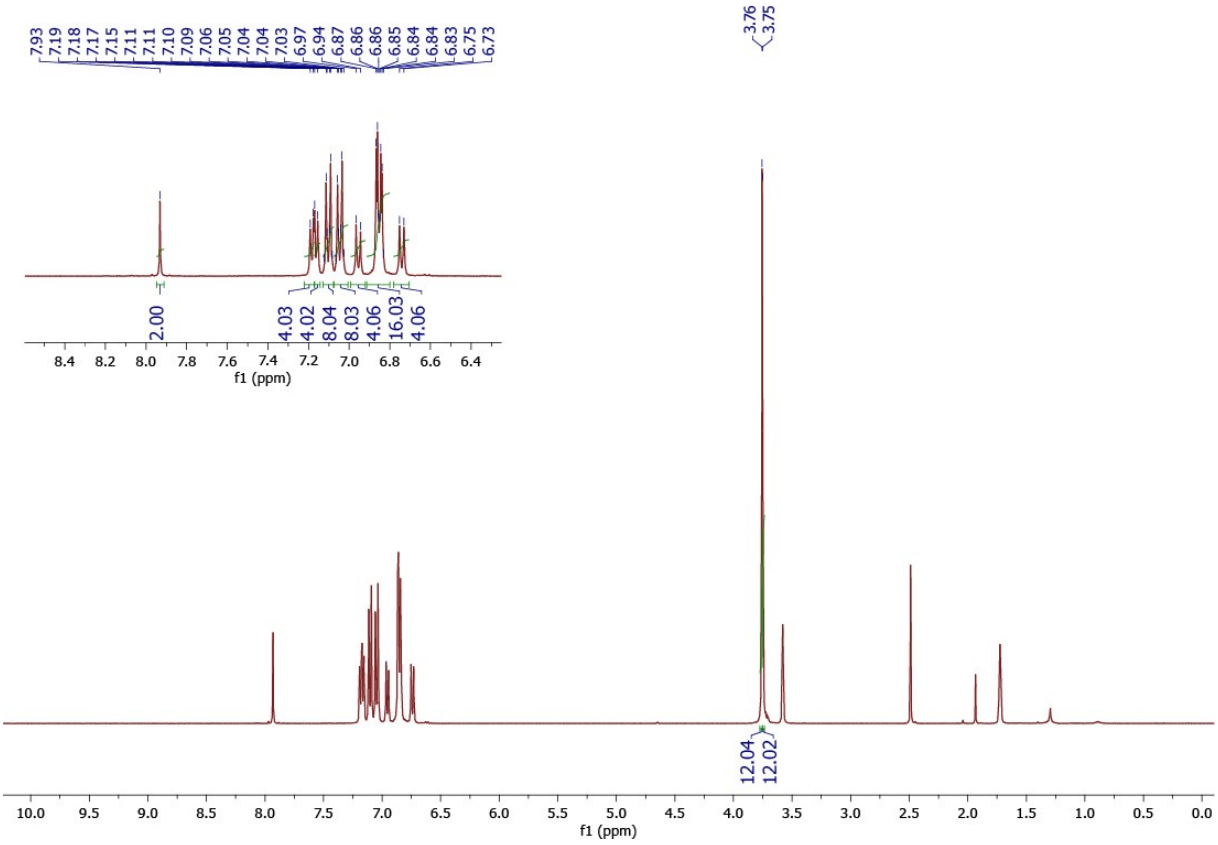

Figure S12. ^{1}H NMR (400 MHz, THF-d_8, 298 K) of compound **TTPA-BDT**.

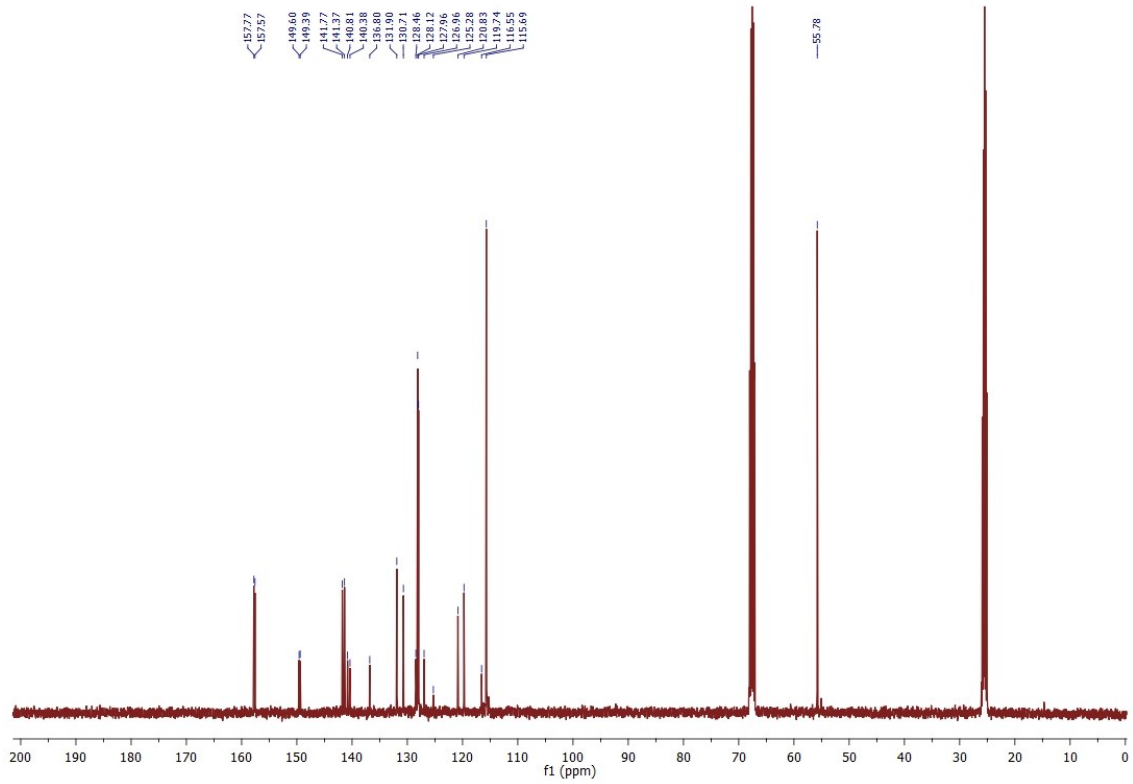

Figure S13. ^{13}C NMR (100 MHz, $CDCl_3$, 298 K) of compound **TTPA-BDT**.

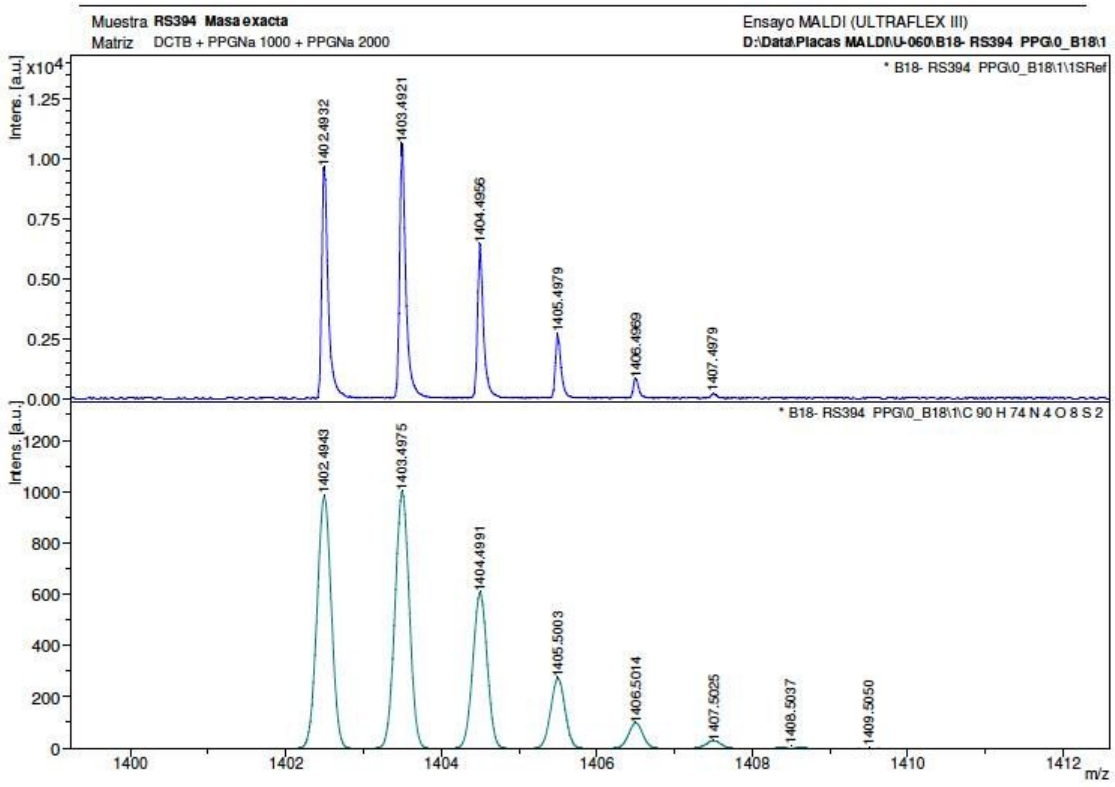

Figure S14. MALDI-TOF mass spectrum of **TTPA-BDT**.

7. References

[1] H.-L. Wong, C.-C. Ko, W. H. Lam, N. Zhu, V. W.-W. Yam, *Chem. Eur. J.* **2009**, *15*, 10005–10009.

[2] Z. Pan, Y. Liu, F. Fan, Y. Chen, Y. Li, X. Zhan, Y. Song, *Chem. Eur. J*. **2013**, *19*, 9771–9774.

[3] P. Ganesan, K. Fu, P. Gao, I. Raabe, K. Schenk, R. Scopelliti, J. Luo, L. H. Wong, M. Gratzel, M. K. Nazeeruddin, *Energy Environ. Sci.* **2015**, *8*, 1986−1991.

[4] Gaussian 09, Revision D.01, M. J. Frisch, G. W. Trucks, H. B. Schlegel, G. E. Scuseria, M. A. Robb, J. R. Cheeseman, G. Scalmani, V. Barone, B. Mennucci, G. A. Petersson, H. Nakatsuji, M. Caricato, X. Li, H. P. Hratchian, A. F. Izmaylov, J. Bloino, G. Zheng, J. L. Sonnenberg, M. Hada, M. Ehara, K. Toyota, R. Fukuda, J. Hasegawa, M. Ishida, T. Nakajima, Y. Honda, O. Kitao, H. Nakai, T. Vreven, J. A. Montgomery, J. E. Peralta, F. Ogliaro, M. Bearpark, J. J. Heyd, E. Brothers, K. N. Kudin, V. N. Staroverov, R. Kobayashi, J. Normand, K. Raghavachari, A. Rendell, J. C. Burant, S. S. Iyengar, J. Tomasi, M. Cossi, N. Rega, J. M. Millam, M. Klene, J. E. Knox, J. B. Cross, V. Bakken, C. Adamo, J. Jaramillo, R. Gomperts, R. E. Stratmann, O. Yazyev, A. J. Austin, R. Cammi, C. Pomelli, J. W. Ochterski, R. L. Martin, K. Morokuma, V. G. Zakrzewski, G. A. Voth, P. Salvador, J. J. Dannenberg, S. Dapprich, A. D. Daniels, Farkas, J. B. Foresman, J. V. Ortiz, J. Cioslowski and D. J. Fox, Gaussian, Inc., Wallingford CT, 2009.

[5] a) C. Lee, W. Yang and R. G. Parr, *Phys. Rev. B*, 1988, **37**, 785–789; b) A. D. Becke, *J. Chem. Phys.* **1993**, *98*, 5648–5652.

[6] M. M. Francl, W. J. Pietro, W. J. Hehre, J. S. Binkley, M. S. Gordon, D. J. Defrees and J. A. Pople, *J. Chem. Phys.*, 1982, **77**, 3654–3665.

[7] a) J. Tomasi and M. Persico, *Chem. Rev.*, 1994, **94**, 2027–2094; b) J. Tomasi, B. Mennucci and R. Cammi, *Chem. Rev.*, 2005, **105**, 2999–3093; c) C. S. Cramer and D. G. Truhlar, in: Solvent Effects and Chemical Reactivity (Eds.: O. Tapia, J. Bertrán), Kluwer, Dordrecht, The Netherlands, 1996, p. 1–80.

[8] a) M. E. Casida, C. Jamorski, K. C. Casida and D. R. Salahub, *J. Chem. Phys.*, 1998, **108**, 4439–4449; b) C. Jamorski, M. E. Casida and D. R. Salahub, *J. Chem. Phys.*, 1996, **104**, 5134–5147; c) M. Petersilka, U. J. Gossmann and E. K. U. Gross, *Phys. Rev. Lett.*, 1996, **76**, 1212–1215.

[9] http://www.chemcraftprog.com

[10] F. Giordano A. Abate, J.P. Correa-Baena, M. Saliba, T. Matsui, S. H. Im, S. M. Zakeeruddin, M. K. Nazeeruddin, A. Hagfeldt and M. Graetzel, *Nat. Commun.*, 2016, **7**, 10379.

[11] N. J. Jeon, J. H. Noh, Y. C. Kim, W. S. Yang, S. Ryu and S. I. Seok, *Nat. Mater.*, 2014, **13**, 897.